Measurement and analysis of x-ray absorption in Al and MgF_2 plasmas heated by *Z*-pinch radiation

Gregory A. Rochau,[1] J. E. Bailey,[1] and J. J. MacFarlane[2]
[1]*Sandia National Laboratories, Albuquerque, New Mexico 87185, USA*
[2]*Prism Computational Sciences, Madison, Wisconsin 53704, USA*
(Received 15 July 2005; revised manuscript received 10 October 2005; published 14 December 2005)

High-power *Z* pinches on Sandia National Laboratories' *Z* facility can be used in a variety of experiments to radiatively heat samples placed some distance away from the *Z*-pinch plasma. In such experiments, the heating radiation spectrum is influenced by both the *Z*-pinch emission and the re-emission of radiation from the high-*Z* surfaces that make up the *Z*-pinch diode. To test the understanding of the amplitude and spectral distribution of the heating radiation, thin foils containing both Al and MgF_2 were heated by a 100–130 TW *Z* pinch. The heating of these samples was studied through the ionization distribution in each material as measured by x-ray absorption spectra. The resulting plasma conditions are inferred from a least-squares comparison between the measured spectra and calculations of the Al and Mg $1s \rightarrow 2p$ absorption over a large range of temperatures and densities. These plasma conditions are then compared to radiation-hydrodynamics simulations of the sample dynamics and are found to agree within 1σ to the best-fit conditions. This agreement indicates that both the driving radiation spectrum and the heating of the Al and MgF_2 samples is understood within the accuracy of the spectroscopic method.

DOI: 10.1103/PhysRevE.72.066405 PACS number(s): 52.25.Os, 52.40.Db, 52.59.Qy, 52.70.La

I. INTRODUCTION

The interaction of x-ray radiation with matter is an important process for many high energy-density physics applications. Measurements of these interactions are crucial for benchmarking computational models of energy transfer via radiation. Examples of experiments that require such computational models include inertial confinement fusion, laboratory astrophysics, and general studies in atomic opacity and/or radiation flow [1–3].

One of the primary challenges in these experiments is the determination of the plasma conditions. A well-established method for diagnosing the local plasma temperature and density is to measure the $1s \rightarrow 2p$ absorption spectrum of radiation passing through the plasma [4–6]. Because different charge states of an atom absorb different x-ray wavelengths, spectrally resolving the radiation absorption provides a signature of the relative ionizations states at the time the spectrum was observed. The absorption spectrum can then be related to the possible temperatures and densities in the plasma by detailed calculations of the atomic energy levels and transition probabilities in combination with the local collisional and radiative ionization rates. The plasma conditions deduced from the experimental spectra must then be compared with radiation-hydrodynamics simulations in order to test the understanding of the physical processes occurring in the experiment.

In the past few decades, high-power lasers have been the primary driver for producing radiatively heated plasmas, and a number of experiments have been conducted to measure the resulting plasma conditions using absorption spectroscopy [4–8]. Recently, high-power *Z* pinches at the Sandia National Laboratories' *Z* facility have been investigated as a radiation driver for conducting similar experiments [9–12]. In this case, the intense burst of radiation from the *Z* pinch acts as both the radiation driver and the x-ray backlighter [12]. This configuration allows for cm-scale samples driven by flux-equivalent radiation temperatures of up to 70 eV in a 5–10 ns full width at half maximum (FWHM) pulse. This drive pulse comes from a *Z*-pinch source that lasts many tens of ns with a radiation spectrum peaking at a brightness temperature of ~150–250 eV.

Figure 1 shows a top-view and a side-view schematic of the geometry used for <70 eV radiation science experiments on the *Z* facility. The sample is placed a distance *d* away from the *Z*-pinch axis along a line-of-sight outside the 1–2 cm radius primary *Hohlraum* (typically made of Au or steel). The *Hohlraum* is also the anode of the *Z*-pinch diode and, therefore, acts as the return path of current. Magnetic field considerations suggest that the sample must be placed at a distance >1 cm from the *Hohlraum* to prevent impacting the *Z*-pinch load dynamics. In this configuration, the driving radiation on the sample surface comes from both the *Z*-pinch emission and the reemission from the hot high-*Z* surfaces that make up the *Z*-pinch diode. The design of experiments using this geometry is complicated by the lack of an integrated computational capability that can simulate the *Z*-pinch implosion, the heating of the three-dimensional diode, and the resulting spectra at the sample location.

MacFarlane *et al.* reported on a method for calculating the radiation drive spectra using a combination of the measured *Z*-pinch power emission and view-factor simulations [9]. They have also reported on an application of this technique to the radiative heating of a thin Al foil [9]. In their experiment, the foil was attached directly to the *Z*-pinch primary *Hohlraum*, and the sample conditions were probed through measurements of the Al $1s \rightarrow 2p$ absorption spectra. In that study, the sample had a different field-of-view than the more general case where the sample is placed >1 cm away from the *Hohlraum*. It is important to test the techniques of Mac-

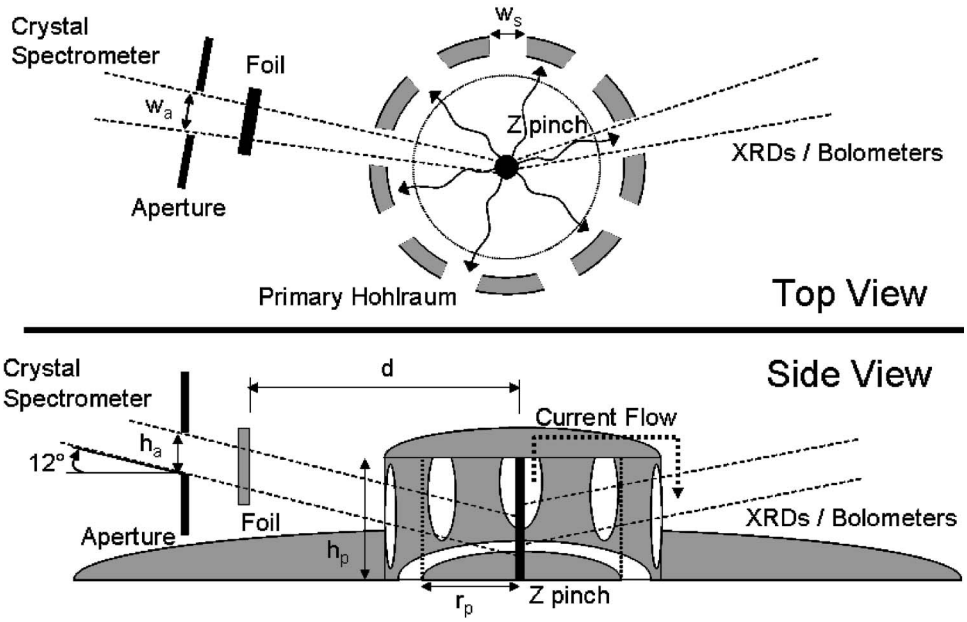

FIG. 1. Schematic diagram of the *Z*-pinch diode and sample placement for <70 eV radiation science experiments on the *Z* facility.

Farlane *et al.* for different geometries in experiments that validate the calculated radiation drive. Such experiments can be most effective if they employ samples containing multiple materials that will be heated by varying parts of the driving radiation spectra. Probing the conditions of each element independently provides a tighter constraint on the calculation of the radiation spectra than probing any one element alone.

This paper reports on the investigation of the radiation absorption in samples containing Al and MgF_2 that are heated by 100–130 TW *Z* pinches. These materials are chosen because each is used as an indicator of the local plasma conditions in experiments on both opacity and radiation flow. Therefore, this work is motivated by the need to validate the simulation capability of both the driving radiation spectra and the radiative energy transfer, and to validate the diagnostic techniques and analysis tools for application in future radiation science experiments.

Section II describes two experiments that were fielded at the *Z* facility to study the radiative heating of thin Al and MgF_2 foils. The plasma conditions are inferred from the atomic charge-state distribution as measured through x-ray absorption by K-α satellite transitions in the samples. In one experiment, measurements were made on a single sample that had Al and MgF_2 mixed together. This experiment was used to verify that the analysis of the absorption spectra from each element (Al and Mg) yields the same range of plasma conditions. In the other experiment, two samples were studied that had the Al and MgF_2 deposited in separate layers. In one sample, the Al was deposited directly in front of the MgF_2 (with respect to the direction of the heating radiation). In the other sample, the MgF_2 was deposited directly in front of the Al. This experiment was used to study the heating of each material in a situation where the materials may not be in collisional equilibrium, and where each material is exposed to a radiation spectrum that has passed through the other material. Section III presents the data from these two experiments along with a least-squares numerical comparison between the experimental spectra and calculations of the $1s \rightarrow 2p$ absorption over a range of temperatures and densities. Section IV describes the computational modeling of the experiments including the calculations of the radiation drive spectra, the radiation hydrodynamics of the sample response, and the detailed spectral post-processing of the radiation-hydrodynamics calculations. Finally, Sec. V summarizes the results and discusses their impact on future radiation science experiments at the *Z* facility.

II. EXPERIMENTS

The *Z* radiation source is a "fast" *Z* pinch produced from 120–360 ~7–12 μm diameter tungsten wires strung side by side in a cylindrical array at a typical radius of 10–20 mm [13–15]. The *Z*-pinch implosion is driven by a ~100 ns wide current pulse peaking at 20 MA, which produces a x-ray pulse with a ~90-ns foot rising from 10–60 eV and a 5–10 ns FWHM primary pulse peaking at ~150–250 eV. The total x-ray output contains 0.5–1.5 MJ of total energy with peak powers of 50–200 TW. As shown in Fig. 1, the return path of the current in the *Z* diode acts as a primary *Hohlraum* that is made of a high-*Z* material and traps a fraction of the radiated pinch energy. This primary has multiple line-of-sight (LOS) holes (also called radiation exit holes) that allow a diagnostic view of the *Z*-pinch plasma. Radiation escaping from the primary can be used to heat samples placed outside these LOS, which is the geometry used in the experiments described here.

The physical parameters of the *Z*-pinch geometry and sample placement for the experiments described in the present work are listed in Table I. These parameters are also shown in Fig. 1 and are defined as the wire-array height h_p, the initial wire-array radius r_p, the primary *Hohlraum* radius r_c, the width of the LOS holes w_h, the distance from the *Z*-pinch axis to the experimental sample d, the aperture width w_a, and the aperture height h_a.

Figures 2(a) and 2(b) show schematics of the sample geometry on experiments $z597$ and $z1031$, respectively. The

TABLE I. Geometric parameters and *Z*-pinch configurations for the experiments numbered *z*597 and *z*1031. Experiment *z*597 was a single array tungsten *Z* pinch with no central target, and *z*1031 was a nested array tungsten *Z* pinch with a 3 mm radius, 14 mg/cc CH_2 axial foam target.

Shot No.	r_p (mm)	h_p (mm)	Wire No.	Wire Diam.	w_s (mm)	d (mm)	w_a (mm)	h_a (mm)
*z*597	10	10	300	11.4 μm	5.6	39.6	8.26	2.49
*z*1031	20 outer	12	240 outer	7.8 μm	4.8	43.3	4	6
	10 inner		120 inner					

experimental sample on *z*597 consisted of seven alternating layers of 200 Å-thick Al or MgF_2, creating a 2800 Å-thick "mixed" Al/MgF_2 foil tamped on both sides by 1.2 μm of CH. Experiment *z*1031 had two different samples fielded simultaneously on two separate LOSs. One sample consisted of a 1500 Å-thick layer of Al on the *Z*-pinch facing side of a 1000 Å layer of MgF_2. The other sample contained a 3100 Å layer of MgF_2 on the *Z*-pinch facing side of a 1500 Å layer of Al. Each of these samples was tamped on both sides by 1.0 μm of CH.

As indicated in Fig. 1, absorption spectra from these samples were measured along each sample's LOS by a time-integrated convex crystal spectrometer. The spectrometers were fielded with a source-to-crystal distance of 4550 mm, and a crystal-to-film distance of 81 mm. Each contained a potassium acid phlalate (KAP) crystal with a $2d$ spacing of 26.62 Å. These crystals were bent to a 101.6-mm radius, which provided a spectral range of ~5–11 Å at a resolution of $\lambda/\Delta\lambda \sim 850$. To both protect the crystals and eliminate the lower energy components of the x-ray spectrum, the spectrometers were filtered between the source and crystal by 38.1 μm of Be on *z*597 and 8.5 μm of Be on *z*1031.

The *Z*-pinch performance on these experiments was measured by a suite of diagnostics looking through LOS other than those used by the experimental samples [16–19]. The primary *Z*-pinch diagnostics utilized for these experiments were an array of filtered x-ray diodes (XRDs), which provided the *Z*-pinch power history when normalized by a bolometer viewing from the same angle [20].

III. RESULTS

Figure 3 shows the time-dependent *Z*-pinch powers and emission temperatures from experiments *z*597 and *z*1031. The time axis in this figure, and throughout the remainder of this paper, has been shifted so that the peak of the x-ray emission power occurs at 100 ns. The powers are determined from Kimfol filtered XRD measurements that have been normalized by bolometer data [19]. According to this data, the *Z*-pinch emission from *z*597 produced 1140 kJ in a 6.6 ns FWHM pulse peaked at ~124 TW. The emission from *z*1031 produced 870 kJ in a ~3.7 ns FWHM pulse peaked at 110 TW. The bolometer normalization method has been reported in a previous work to be accurate to 20% in power [20].

The emission temperatures for both experiments are calculated from the *Z*-pinch power and radius time histories assuming that the *Z* pinch is a uniform cylindrical surface emitter. This method has been compared to transmission grating measurements of the *Z*-pinch emission spectra on similar experiments and was found to be in agreement [20,21]. For the emission temperature calculation, the

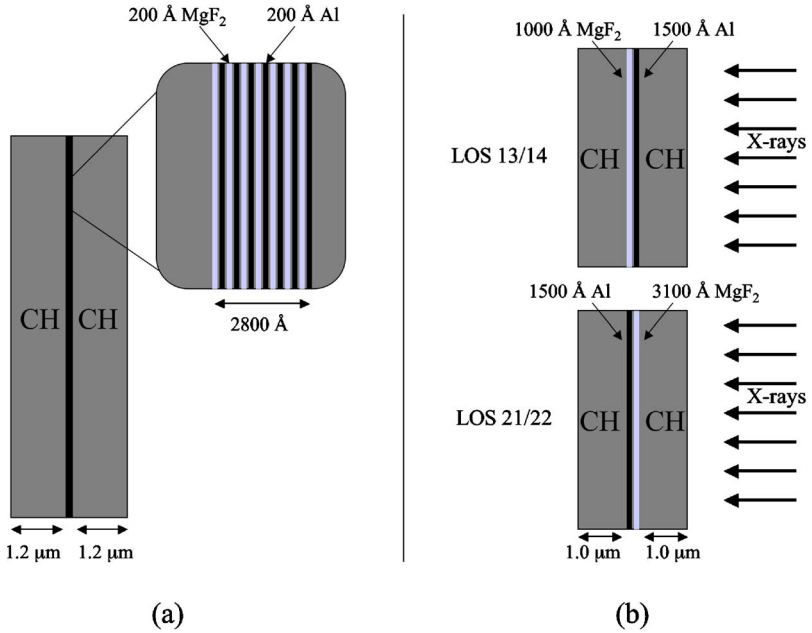

FIG. 2. (Color online) Schematic drawings of the samples used on experiments (a) *z*597 and (b) *z*1031.

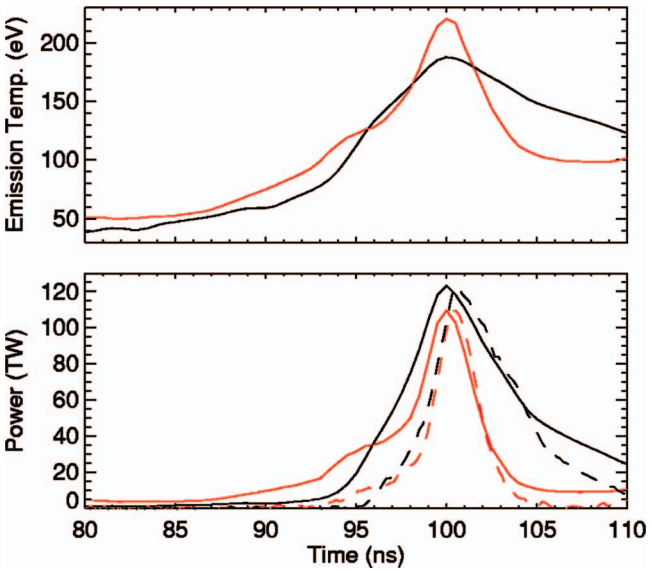

FIG. 3. (Color) *Z*-pinch power and emission temperature on experiments *z*597 (black solid) and *z*1031 (red solid). Also shown are the time histories of the backlighter x-ray emission in the range 2.5 Å $\leqslant \lambda \leqslant$ 12.4 Å on *z*597 (black dashed) and *z*1031 (red dashed). The backlighter histories have been normalized to the peak of the x-ray emission powers.

Z-pinch radii are determined from models of the implosion trajectory at times $<$93 ns [22,23] and from experimental data on similar geometries at later times [24,25]. The minimum *Z*-pinch radii occur at the time of peak *Z*-pinch emission and were determined to be $\sim$1.5 mm and $\sim$0.6 mm on *z*597 and *z*1031, respectively. The resulting *Z*-pinch emission temperatures are calculated to reach a peak of $\sim$190 eV on *z*597 and $\sim$220 eV on *z*1031.

In addition to the total *Z*-pinch emission power, the XRD data also provides information about the backlighter time history. Overlaid on the power histories in Fig. 3 are measured signals from a XRD that is filtered by 10 μm of beryllium and 0.8 μm of vanadium (the signals have been normalized to the peak of the total x-ray power). The combination of the XRD sensitivity and the filter transmission fraction makes the Be/V filtered XRD a diagnostic of the *Z*-pinch emission over the range 2.5 Å $\leqslant \lambda \leqslant$ 12.4 Å. This covers the range of the spectrometers used to measure the Al and MgF_2 absorption spectra in these experiments. The time history of the emission in this spectral range is more narrow than the total *Z*-pinch power emission and is slightly delayed from the peak of the main power pulse. The FWHM of the emission in the spectral range of the spectrometers is measured to be 4.0 ns on *z*597 and 2.8 ns on *z*1031. Each signal peaks 0.5 ns after the peak of the heating pulse, a delay that is outside the 0.1 ns error in cross timing between XRDs in the same diagnostic head.

The spectra as recorded by the convex crystal spectrometers on *z*597 and *z*1031 are shown in Fig. 4. The data has been corrected for the filter transmission [26], the crystal reflectivity (using a modified Darwin-Prins reflectivity model) [27], and the crystal geometry [28]. These absorption spectra can be used to derive the possible combinations of temperature and density in the foils through calculations of the charge-state distribution and associated energy level populations.

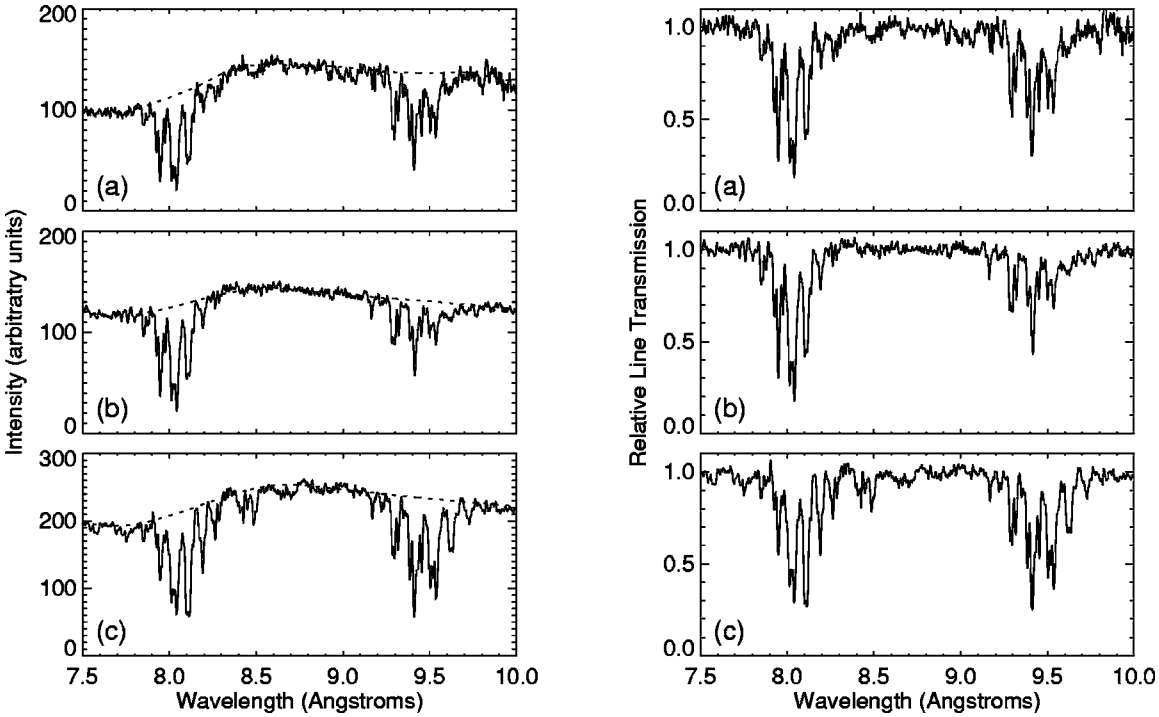

FIG. 4. Al and Mg absorption spectra recorded through the (a) mixed Al/MgF_2 on *z*597, (b) the Al-first foil on *z*1031, and (c) the MgF_2-first foil on *z*1031. The figures on the left show the spectra in relative intensity units overlaid by the assumed continuum (dashed). The figures on the right show the relative line transmission after dividing each spectrum by the continuum.

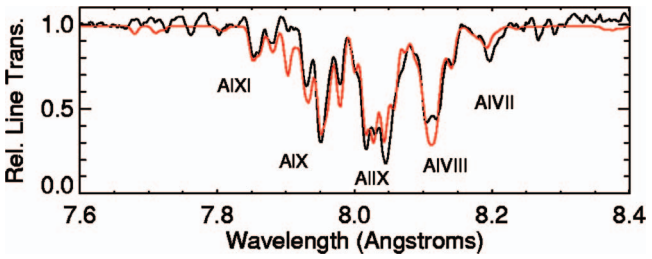

FIG. 5. (Color) Example of the quality-of-fit in the χ_ν^2 fitting procedure for the Al-first sample on $z1031$. The simulated Al transmission (red) is shown for an assumed ion density of 3.7×10^{20} cm^{-3} and a temperature of 37.5 eV.

A direct measure of the backlighter spectra was not possible on these experiments. Thus, the spectra must be converted to a relative line transmission by the division of an assumed continuum. That continuum was determined by removing the absorption features from the efficiency corrected spectral lineouts, and then filtering the remaining signal by a low-pass filter. The relative transmission was then calculated by dividing the measured signal by this continuum. This is considered an acceptable procedure since the important information about the sample conditions is contained in the relative intensities of the absorption features, which are relatively unchanged by the division of the continuum. The plots in Fig. 4 show the original spectra, the assumed continua, and the relative line transmission from each sample.

The plasma conditions can then be determined by computing a weighted chi squared between the measured transmission spectra and those simulated by a detailed spectral analysis code [29]. A range of plasma conditions must be considered because the absorption spectra can be similar for different combinations of temperature and density. This degeneracy exists because the temperature-dependent and density-dependent linewidth effects are not observable over the resolution of the spectrometers. For this analysis, the reduced chi squared χ_ν^2 between the transmission data and calculated spectra were computed for 1800 combinations of temperature and density over the ranges $20\ \text{eV} \leqslant T_e \leqslant 80$ eV and $10^{19}\ \text{cm}^{-3} \leqslant n_i \leqslant 10^{23}\ \text{cm}^{-3}$. The calculations were done assuming local thermodynamic equilibrium (LTE) with PRISMSPECT [30], a spectral analysis code that uses detailed term accounting (DTA) atomic physics to compute x-ray line absorption. These models used fine structure atomic energy level detail for principle levels $n \leqslant 3$, L-S term splitting for levels $4 \leqslant n \leqslant 5$ and configuration averaging for levels $n > 5$. In the computation of χ_ν^2, the statistical deviations of each point in the data were determined from independent experiments [31]. Each comparison was restricted to the $1s \rightarrow 2p$ transitions, which were considered to be $7.75\ \text{Å} \leqslant \lambda \leqslant 8.34$ Å for the Al spectra and $9.15\ \text{Å} \leqslant \lambda \leqslant 9.9$ Å for the Mg spectra.

To illustrate the quality of the fit between the data and calculations, Fig. 5 overlays the aluminum absorption spectrum from the Al-first sample on $z1031$ with the PRISMSPECT point calculation at an ion density of 3.7×10^{20} cm^{-3} and a temperature of 37.5 eV. The χ_ν^2 between these two spectra is ~ 1.2. The good agreement between the data and the point calculation indicates that it is acceptable to use a uniform plasma approximation in computing the spectra for the χ_ν^2 comparisons. This does not necessarily imply that the plasma is uniform, but rather the effects that any temperature and density gradients have on the spectrum are small compared to the statistical fluctuations in the data. Calculations that include gradients may give similar χ_ν^2, but are considered an unnecessary complication and outside the scope of the present work.

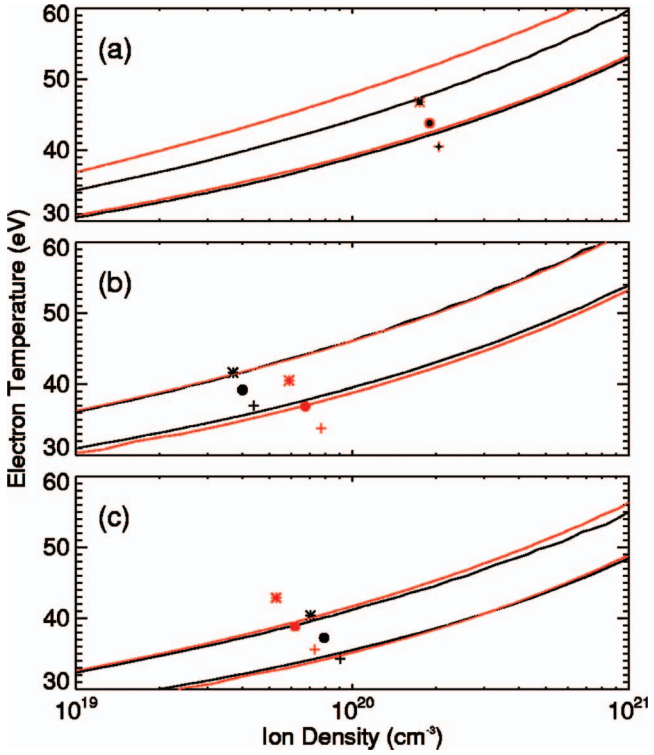

FIG. 6. (Color) 1σ contour plots from chi-squared fitting between the experimental data and synthetic spectra of the aluminum (black) and magnesium (red) in (a) the mixed foil on $z597$, (b) the Al-first foil on $z1031$, and (c) the MgF_2-first foil on $z1031$. The symbols correspond to the mass-averaged conditions of the aluminum (black) and magnesium (red) calculated with one-dimensional radiation-hydrodynamics computer simulations. The simulations were time averaged with a weighting function determined from the backlighter time history. The dots correspond to simulations using the nominal measured Z-pinch output power to infer the sample heating, while the crosses and stars correspond to simulations using 80% and 120% of the nominal Z-pinch power, respectively.

Figure 6 shows the resulting contour plots of the 1σ uncertainties in the χ_ν^2 comparisons across a large range of the temperature-density phase space considered in the calculations. Assuming that the distribution in the measured intensity of each data point follows Gaussian statistics, there is a $\sim 68\%$ probability that the spectra correspond to a plasma at a temperature and density within the contours. The production of these plots is a new development in the field of tracer absorption spectroscopy and provides a quantitative picture of the possible plasma conditions as determined only from the measured spectra.

The contours in Fig. 6 reveal important information about the relative temperatures and densities of each material. The contours in Fig. 6(a) correspond to the conditions of the

mixed Al and MgF_2 foil and indicate that the Al and Mg have a statistically equivalent combination of temperature and density. This should be the case for a foil whose constituents are in thermodynamic equilibrium. The contours in Figs. 6(b) and 6(c) show a similar result. These correspond to the conditions of the samples that had the Al and MgF_2 in a swapped sequence along the direction of the heating radiation. One might expect the material that is first in the sequence to have a higher temperature than the one behind it. However, the figure indicates that the possible range of plasma conditions are statistically equivalent for both the Al and MgF_2 in each sample. Because the contours are defining a phase space of constant ionization, a higher temperature in one of the tracers must be accompanied by a higher density. Conversely, in a plasma that is free to expand (and in the absence of any shocks), equation-of-state arguments require that a higher temperature must be accompanied by a lower density. Therefore, the most likely result is that the two tracers have similar temperatures. As discussed in Sec. IV, this can occur because the two materials have different frequency-dependent opacities and couple to different parts of the radiation drive spectra.

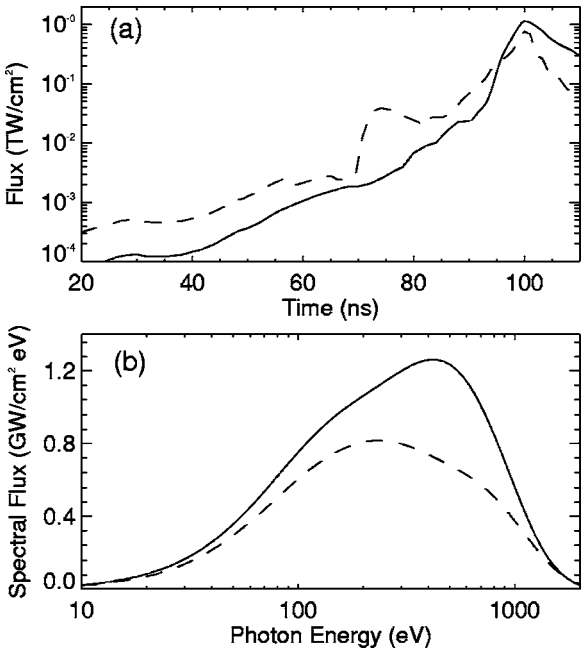

FIG. 7. Calculated (a) radiation drive flux and (b) peak drive spectrum (at $t=100$ ns) for experiments $z597$ (solid) and $z1031$ (dashed).

IV. RADIATION-HYDRODYNAMICS CALCULATIONS

Modeling these experiments requires a calculation of the radiation drive on the surface of each sample. The *Z*-pinch diode is constructed of high-*Z* (gold and/or steel) anode and cathode surfaces, which are heated by the *Z*-pinch source and re-emit a fraction of the heating radiation. Since these surfaces are in the field-of-view of the experimental samples, their contribution to the drive radiation must be included. MacFarlane *et al.* [32] have developed a method using view-factor calculations [33] to determine the total drive spectra on the experimental sample from all the surfaces (including the *Z* pinch) that are within the field-of-view of the experimental sample. This method uses the experimentally measured *Z*-pinch radius and emission power as inputs, and an assumed albedo of each diode surface. The albedos are calculated for each representative surface using the BUCKY radiation-hydrodynamics code [34]. Since the albedos depend on the result of the view-factor calculation and the view-factor calculation depends on the albedos, the calculations must be iterated until the x-ray flux at the sample has converged. The resulting spectra calculated at the sample surface are a combination of the *Z*-pinch emission blackbody and the emission blackbody of the many different surface temperatures in view of the sample.

Using this method, the time-dependent and frequency-dependent radiation intensity was computed for the samples on experiments $z597$ and $z1031$. The resulting radiation flux histories are shown in Fig. 7(a) and have a peak flux of 1.15 TW/cm^2 on $z597$ and 0.76 TW/cm^2 on $z1031$. The calculated radiation drive spectra at peak flux are shown in Fig. 7(b) for each experiment. The peak photon energy of these spectra is 410 eV on $z597$ and 235 eV on $z1031$. The lower peak energy of the drive on $z1031$ is due to the greater amount of gold surface area in the sample's field-of-view, which radiates at a lower temperature than the *Z* pinch. The "bump" on the incident flux at $t\approx 75$ ns on $z1031$ is from an increase in the *Z*-pinch emission when the outer array of wires interacts with the inner array. The *Z* pinch on $z597$ was composed of only a single array and, therefore, shows no such feature.

The radiation drive histories from Fig. 7(a) were applied as a time-dependent and frequency-dependent radiation boundary condition in radiation-hydrodynamics (rad-hydro) calculations of the sample response. These simulations were done with the BUCKY one-dimensional (1D) Lagrangian rad-hydro code [34] using multiangle short-characteristics radiation transport [35] for 100 logarithm-spaced photon energy groups from 0.1 to 10^4 eV. The opacities of each material were taken from a table look-up of DTA calculations [30] at 39 temperature points from 0.1 to 100 eV and 41 logarithm-spaced density points from 10^{19} to 10^{23} cm^{-3}. The equations-of-state (EOSs) for the CH and Al materials were taken from the SESAME EOS tables, and those for the MgF_2 and Al/MgF_2 materials were taken from quotidian EOS (QEOS) calculations. The rad-hydro models were begun at $t=0$ ns and ended at a time of 110 ns. These calculations were then repeated for each sample assuming the *Z*-pinch power was 20% lower and then 20% higher than the nominal measured power. This was done to account for the uncertainty in the *Z*-pinch power measurements, which have been shown elsewhere to be the dominant uncertainty in the calculated radiation drive [36].

The calculated conditions in the Al and MgF_2 foils are shown on the χ^2_ν contour plots in Fig. 6. These points are overplotted on each contour plot as a large symbol corresponding to assumed *Z*-pinch powers of 80%, 100%, and 120% of the nominal value. In each calculation, the plasma conditions are mass averaged over the extent of the Al and/or MgF_2 plasma and time averaged using the backlighter power

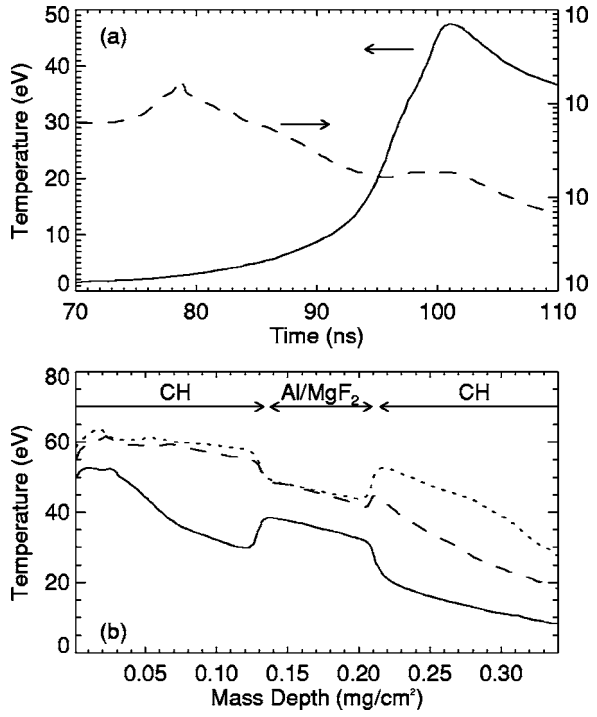

FIG. 8. (a) Simulated mass-averaged temperature (solid) and density (dashed) conditions in the Al/MgF_2 foil on $z597$. (b) Simulated temperature profiles in the Al/MgF_2 foil at times of 98 ns (solid), 100 ns (dashed), and 102 ns (dotted).

history from Fig. 3 as a weighting function. The calculations are shown in this way because it provides a quick visual way to compare to the data. As seen in Fig. 6, the simulated conditions of each sample fall within the 1σ contours of the experimental data for an assumed *Z*-pinch power within 20% of the measured value.

A. Calculations in mixed Al and MgF_2

For clarity, first consider the calculations in the mixed Al and MgF_2 sample from $z597$. The agreement between the experimental and simulated plasma conditions in Fig. 6 provides confidence that the view-factor calculation and rad-hydro model together predict temperature and density conditions in the sample that are consistent with the measured values. With this constraint in place, the models can be used to investigate the dynamics in the sample.

Figure 8 shows some details of the conditions calculated by the rad-hydro model assuming a pinch power that is 10% higher than that determined from the XRD/bolometer analysis. This higher power is used because the resulting plasma conditions are in best agreement with the data (minimum χ^2 in Fig. 6) and is well within the uncertainties of the *Z*-pinch power diagnostics. Figure 8(a) shows the time history of the mass-averaged temperature and density in the Al/MgF_2 layer (the electron and ion temperatures are in equilibrium). The temperature peaks at about 47 eV at a time of 101 ns, while the density decreases to a value of about 1.7×10^{20} cm^{-3} and remains approximately constant over times of 97 ns $< t <$ 103 ns. Figure 8(b) shows the temperature profiles in the sample at times of 98 ns, 100 ns, and 102 ns. At each time, the calculations predict a $\sim$5 eV gradient in the temperature of the Al/MgF_2 and almost no gradient in the density. One point of interest in these calculations is the noticeable jump in the conditions at the interface of the CH tamper and the Al/MgF_2. The Al/MgF_2 is hotter than the surrounding CH at times $<$99 ns and cooler at later times.

The discontinuities in the temperature profiles of the sample can be explained by the frequency-dependent coupling between the driving radiation field and the material opacities. At times of $\sim$80–98 ns, the driving radiation spectra has a large fraction of the total energy at 100 eV $< h\nu <$ 350 eV. This is below the C *K* edge where the opacity of the CH is low, but above the *L* edge of the Al, Mg, and F where the opacity of the Al/MgF_2 foil is high. In this situation, a large fraction of the driving radiation passes through the tamper and is absorbed in the Al/MgF_2. Therefore, the Al/MgF_2 is radiatively heated to a higher temperature than the surrounding CH. At times near the peak of the radiation drive, the incident spectra are peaked around 400–500 eV, which is above the C *K* edge where the opacity of the CH is high. At these times, the CH is more efficiently heated by the incident radiation, and a lower fraction of the total drive spectra reaches the Al/MgF_2. Additionally, the high opacity of the Al/MgF_2 at photon energies around 150 eV makes it a more efficient radiator at the blackbody temperature of the plasma ($\sim$45 eV), which causes it to more quickly cool. This creates a situation where the Al/MgF_2 cools to a temperature lower than the surrounding CH. The CH plasma behind the Al/MgF_2 continues to increase in temperature between 100 ns and 102 ns because, unlike the CH in front of the tracer, the coupling of the opacity to the heating radiation spectrum is higher than the coupling of the opacity to the local emission blackbody. Thus, the absorption rate is still higher than the emission rate, and the plasma heats until it can reach an equilibrium.

There is no direct experimental data to verify the conditions of the CH plasma. The measured absorption spectra are only sensitive to the conditions of the Al/MgF_2 plasma. However, the rad-hydro calculations show that the conditions of the Al/MgF_2 are sensitive to the frequency dependence of the heating radiation, which in turn depends on the conditions of the CH. Properly calculating the conditions of the Al/MgF_2 requires an adequate treatment of the absorption and emission in both the CH and the Al/MgF_2.

While the χ^2_ν fitting in Sec. III provides information on the average conditions in the Al and MgF_2, the experimental spectra contains additional information about the charge-state distribution. The comparison between the measured and simulated charge-state distribution can be made by overlaying the experimental spectra with that from a direct post processing of the simulation. Figure 9 shows this comparison for the mixed Al/MgF_2 foil from experiment $z597$. The simulated spectrum was calculated with the SPECT3D spectral post processing code [30] using a detailed configuration analysis of the Al/MgF_2 atomic level populations and transition probabilities. The spectrum is calculated under an assumption of LTE and has been averaged over the simulated time-dependent spectra using the measured time-dependent intensity of the backlighter as a weighting function. The as-

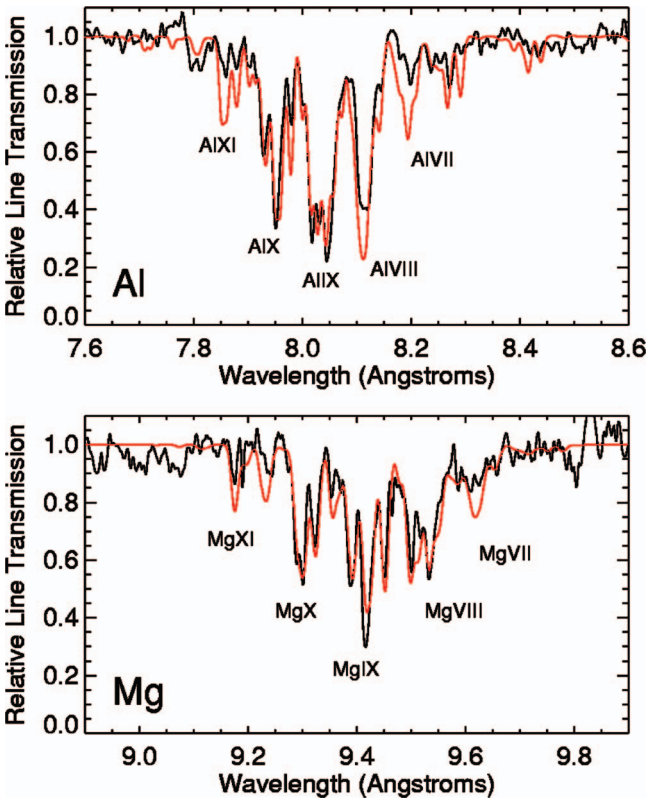

FIG. 9. (Color) Comparison between the measured and simulated (red) relative line transmission in the mixed Al/MgF_2 foil on $z597$. The labeled features correspond primarily to the $1s \rightarrow 2p$ transitions in Al or Mg at the listed ionization state.

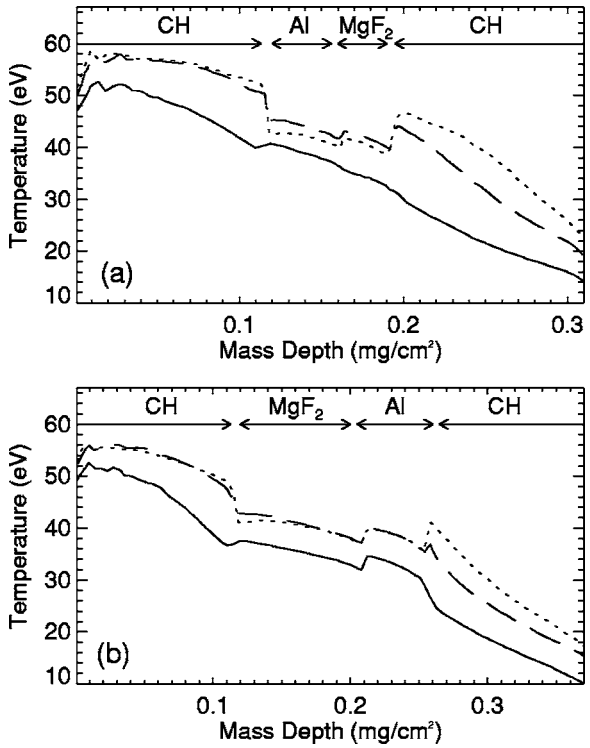

FIG. 10. Calculated temperature profiles at 99 ns (solid), 100.5 ns (dashed), and 102 ns (dotted) in the (a) Al-first and (b) MgF_2-first samples on $z1031$.

sumption of LTE was validated through point calculations of the nonlocal thermodynamic equilibrium (NLTE) populations using a nonlocal treatment of the bound-bound and bound-free photoabsorption rates. These calculations indicate that the collisional ionization rates dominate the Al and Mg atomic level populations in a way consistent with the LTE approximation.

As seen in Fig. 9, the comparison between the measured and simulated spectra is quite good. Qualitatively, the largest deviations between these spectra are in the absorption features of the minimum and maximum charge states. The calculated Al XI, Al VIII, and Al VII $1s \rightarrow 2p$ absorption features are slightly deeper than those observed in the experiment. The same is true for the Mg XI and Mg VII features. This may indicate a slightly larger gradient in the calculated conditions than those in the experiment. Given the long time history of the backlighter, it is not possible to tell whether this discrepancy occurs in time or space. Either way, the differences are small and the authors consider the overall agreement to be acceptable.

B. Calculations in separated Al and MgF_2

The calculated dynamics that occur in the adjacent Al and MgF_2 layers on $z1031$ are very similar to those discussed above. As seen in the contour plots of Fig. 6, the calculated conditions in both samples on $z1031$ are within 1σ of the conditions inferred through the χ^2_ν fitting of the experimental data. These plots show no statistically significant differences in the T-ρ phase space of the Al and MgF_2 foils, irrespective of their order with respect to the heating radiation. It is possible that the temperature in the forward material is higher, but the density would also have to be higher to conserve the ionization state. Assuming the neighboring plasmas must maintain a pressure balance, it is physically improbable that this is the case ($P \propto T\rho$). It is more likely that the two plasmas have very similar average temperatures (and densities), even though each may contain a gradient.

Figures 10(a) and 10(b) show the simulated temperature profiles at times of 99 ns, 100.5 ns, and 102 ns in the Al-first and MgF_2-first samples on $z1031$. As in the discussion from $z597$, there is a small discontinuity in the temperature at the boundary of the foils and the CH tamper. There is also a discontinuity at the boundary between the Al and MgF_2. The temperature at the front of the rear foil is higher than that at the back of the forward foil. Even though the Al and MgF_2 each contain a ~ 5 eV gradient, their average temperatures differ by less than 2 eV.

To demonstrate the frequency-dependent heating that causes this effect, Figs. 11(a) and 11(b) show the frequency-dependent net radiation heating in the Al and MgF_2 from the simulations of each sample at the time of peak drive power. The simulations indicate that the discontinuities in the temperature profiles are caused by different ranges of photoabsorption in the different materials. In both cases, the Al is primarily heated in the range $200\ \text{eV} < h\nu < 300\ \text{eV}$ corresponding to bound-free absorption in the Al L shell. The

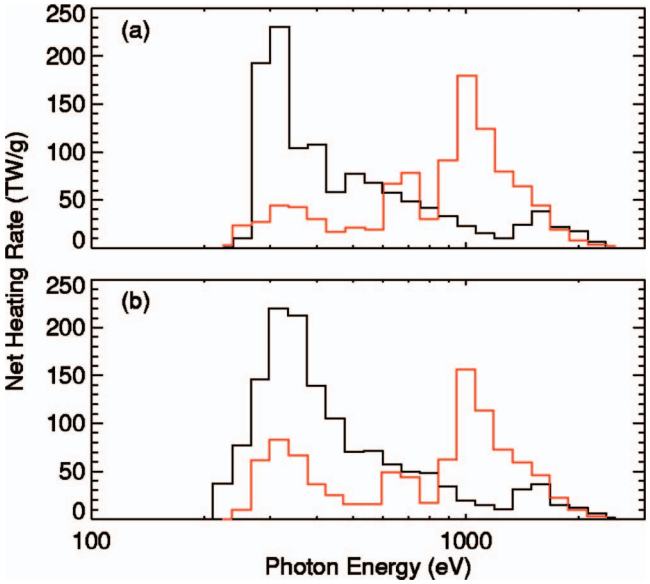

FIG. 11. (Color) Calculated net radiation heating at peak drive power in the Al (black) and MgF_2 (red) layers in the (a) Al-first and (b) MgF_2-first samples on $z1031$.

MgF_2 is primarily heated in the range $900\ \text{eV} < h\nu < 1100\ \text{eV}$ corresponding to bound-free absorption in the F and Mg K shells, with some contribution to the heating around 200 eV corresponding to bound-free absorption in the Mg L shell. The CH absorbs the bulk of the radiation in the range $350\ \text{eV} < h\nu < 450\ \text{eV}$ (corresponding to bound-free absorption in the C K shell) and passes the radiation in the ranges where it is best absorbed by the Al and MgF_2. Since each of the materials is heated by a different range of photon energies, the resulting plasma conditions are similar irrespective of their orientation along the direction of the heating radiation. These dynamics can only be captured by a multifrequency treatment of the radiative transfer.

The good agreement between the simulated and experimental mass-averaged plasma conditions indicates that the combination of the view-factor simulations, calculated opacities, and frequency-dependent radiative transfer are consistent with the measured quantities in the experiments. The contours in Fig. 6 indicate that, at any given density, the spectroscopic method is accurate to ±3.5 eV. At the density calculated for each material, the radiation-hydrodynamics simulations must, therefore, reproduce the corresponding temperature from Fig. 6 to ±3.5 eV in order to agree with the measured spectra. Furthermore, the points plotted on Fig. 6 indicate that a ±20% change in the incident flux changes the simulated electron temperature by $\sim \pm 3.5$ eV with only a small change in density. Given that the Al is primarily heated in the energy band of $200\ \text{eV} < h\nu < 300$ eV, and the MgF_2 is primarily heated in the energy band of $900\ \text{eV} < h\nu < 1100$ eV, then the incident flux in these photon energy bands must be individually modeled to an accuracy of $\sim \pm 20\%$. In addition, if the spectra contained significantly more radiation in the range $h\nu > 1100$ eV, then the Al would heat more through bound-free absorption out of the Al K shell, and the resulting plasma conditions could move above the 1σ contours in Fig. 6. If the spectrum were simply shifted to higher energies (with more radiation at $h\nu > 1100$ eV and less radiation at $h\nu < 300$ eV), the effect of the different photoabsorption bands in the Al and MgF_2 would be diminished. This would cause the forward foil to absorb more of the propagating radiation, and the lower radiative heating in the rear foil could move the conditions out

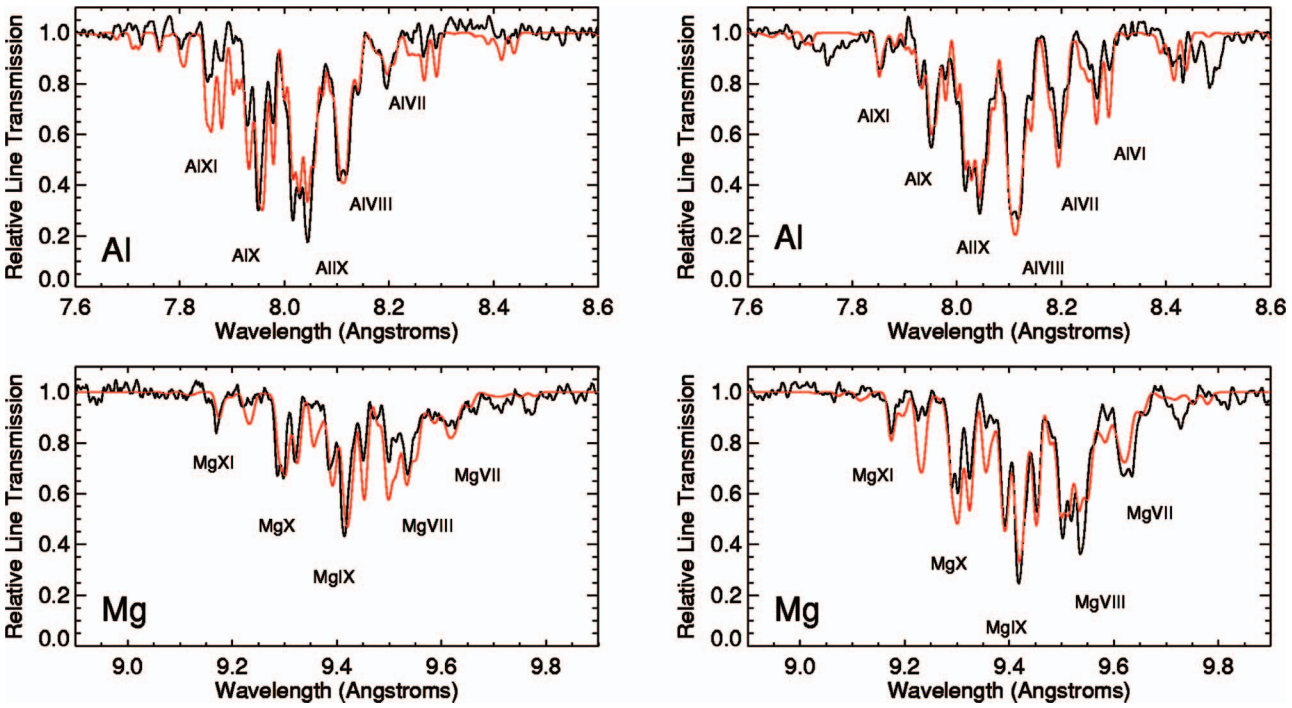

FIG. 12. (Color) Comparison between the measured and simulated (red) relative line transmission in the Al-first (left) and MgF_2-first (right) samples on $z1031$. The labeled features correspond primarily to the $1s \rightarrow 2p$ transitions in Al or Mg at the listed ionization state.

of agreement with those inferred from the experiment. There are many possible permutations of the radiation drive spectra, and it is possible that the spectra used in these calculations do not uniquely produce plasma conditions in agreement with the experiments. However, the combination of the view-factor simulations using the measured *Z*-pinch emission power with radiation-hydrodynamics simulations employing a detailed treatment of the frequency-dependent opacities and radiative transfer provides simulated temperature and density conditions in each tracer that are consistent with the measured quantities.

As a final check on the comparison between the calculated and measured conditions in the Al and MgF_2 foils, the spectral data from each sample on $z1031$ are overlaid by the spectra calculated from the radiation-hydrodynamics simulations in Figs. 12(a) and 12(b). Each spectrum is calculated under an assumption of LTE and is averaged over the time-dependent intensity of the backlighter. The comparison between the measured and calculated spectra is quite good. The largest discrepancy is in the Al XI feature at 7.8–7.9 Å. The calculation overpredicts the depth of this feature, which indicates that the Al is overionized in the calculation (on average). Given that the Al VII feature at the long wavelength end of the Al spectrum is in good agreement, it can be deduced that the calculated ionization gradient in the Al layer is larger than that in the experiment. Since the ionization distribution is much more sensitive to temperature than density, this likely implies that the calculated peak temperatures in the Al sample are too high either in time or space (or both). The correct fix to this calculation should result in a lower average ionization state in the Al without significantly affecting either the Al *X*–Al VII ionization fractions or the ionization distribution of the Mg. There are a large number of permutations on the drive spectra and/or opacities that could cause such a discrepancy. One explanation could be a spectrum at the front of the Al layer that has too many photons at ~300 eV. The rad-hydro calculations show that the heating in the energy bin at 320 eV is a factor of 2 larger at the front of the Al than the back, and contributes ~10% of the total heating at the front of that layer. Thus, the discrepancy between the data and simulation could be caused by a drive spectrum that is slightly too cold, a CH opacity that is slightly too low, or an Al opacity that is slightly too high at ~320 eV. Given the assumptions involved in simulating the experiments and the uncertainties in the measured *Z*-pinch power, the overall comparison between the data and simulations is considered to be acceptable.

V. SUMMARY

Good understanding of the radiative heating and the associated $1s \rightarrow 2p$ absorption features in thin foils of Al and MgF_2 on Sandia's *Z* facility was demonstrated. Given that each experiment discussed in this paper had different *Z*-pinch geometries and incident power histories, these results provide confidence in both the methods used to simulate the frequency-dependent driving radiation spectra and in the physical models applied to simulate the radiation-hydrodynamics processes.

In these experiments, the calculations that successfully reproduce the experimental data indicate that frequency-dependent radiative heating and cooling play the dominant role in determining the time-dependent temperature and density conditions in the samples. This is an important result because it places a restriction on the computational methods that must be used to model the dynamics in similar samples heated by *Z*-pinch radiation. In addition, the role of the radiation field in determining the sample conditions implies that the inferred plasma conditions can be used as an indirect diagnostic of the magnitude and spectral distribution of the radiation field at the location of the tracer plasma (Al and MgF_2). In the future, these materials will be used in *Z*-pinch heated samples as diagnostics of the plasma conditions in radiative transfer and opacity experiments.

ACKNOWLEDGMENTS

The authors thank the *Z* accelerator team for their hard work and dedication in making these experiments possible. We are also grateful to R. J. Leeper, M. K. Matzen, T. A. Mehlhorn, and G. A. Moses for their encouragement and financial support. Sandia is a multiprogram laboratory operated by Sandia Corporation, a Lockheed Martin Company, for the United States Department of Energy under Contract No. DE-AC04-94AL85000.

[1] R. W. Lee *et al.*, Fusion Technol. **30**, 520 (1996).
[2] M. D. Rosen *et al.*, Phys. Plasmas **3**, 1803 (1996).
[3] E. M. Campbell *et al.*, Laser Part. Beams **15**, 607 (1997).
[4] T. S. Perry *et al.*, Phys. Rev. Lett. **67**, 3784 (1991).
[5] T. S. Perry *et al.*, J. Quant. Spectrosc. Radiat. Transf. **54**, 317 (1995).
[6] P. T. Springer *et al.*, Phys. Rev. Lett. **69**, 3735 (1992).
[7] C. A. Back, J. D. Bauer, O. L. Landen, R. E. Turner, B. F. Lasinski, J. H. Hammer, M. D. Rosen, L. J. Suter, and W. H. Hsing, Phys. Rev. Lett. **84**, 274 (2000).
[8] C. Chenais-Popovics *et al.*, J. Quant. Spectrosc. Radiat. Transf. **65**, 117 (2000).
[9] J. J. MacFarlane *et al.*, Phys. Rev. E **66**, 046416 (2002).
[10] R. Heeter *et al.*, in *Proceedings of AIP APIP* (2000), p. 111.
[11] J. E. Bailey *et al.*, J. Quant. Spectrosc. Radiat. Transf. **71**, 157 (2001).
[12] J. E. Bailey *et al.*, Phys. Plasmas **9**, 2186 (2003).
[13] M. K. Matzen, Phys. Plasmas **4**, 1519 (1997).
[14] R. Spielman *et al.*, Phys. Plasmas **5**, 2105 (1998).
[15] C. Deeney, M. R. Douglas, R. B. Spielman, T. J. Nash, D. L. Peterson, P. L. E. Plattenier, G. A. Chandler, J. F. Seamen, and K. W. Struve, Phys. Rev. Lett. **81**, 4883 (1998).
[16] R. Spielman *et al.*, Rev. Sci. Instrum. **68**, 782 (1997).
[17] L. E. Ruggles *et al.*, Rev. Sci. Instrum. **68**, 1063 (1997).

[18] G. A. Chandler *et al.*, Rev. Sci. Instrum. **70**, 561 (1999).
[19] T. J. Nash *et al.*, Rev. Sci. Instrum. **72**, 1167 (2001).
[20] M. E. Cuneo *et al.*, Phys. Plasmas **8**, 2257 (2001).
[21] M. E. Cuneo *et al.*, Laser Part. Beams **19**, 481 (2001).
[22] S. V. Lebedev, F. N. Beg, S. N. Bland, J. P. Chittenden, A. E. Dangor, M. G. Haines, S. A. Pikuz, and T. A. Shelkovenko, Phys. Rev. Lett. **85**, 98 (2000).
[23] G. A. Chandler *et al.*, *IEEE International Pulsed Power Conference*, 2001 (unpublished).
[24] T. W. Sanford *et al.*, Phys. Plasmas **9**, 3573 (2002).
[25] M. Mazarakis (private communication).
[26] F. Biggs and R. Lighthill, Sandia National Laboratories, Report No. SAND87-0070, 1987 (unpublished).
[27] B. L. Henke (private communication).
[28] B. L. Henke *et al.*, Rev. Sci. Instrum. **54**, 1311 (1983).
[29] P. R. Bevington, *Data Reduction and Error Analysis for the Physical Sciences* (McGraw-Hill, New York, 1992).
[30] J. J. MacFarlane *et al.*, in *Proceedings of Inertial Fusion Sciences Applications*, 2004 (unpublished).
[31] G. S. Dunham *et al.*, Rev. Sci. Instrum. **75**, 3687 (2004).
[32] J. J. MacFarlane *et al.*, Rev. Sci. Instrum. **72**, 1228 (2001).
[33] J. J. MacFarlane *et al.*, J. Quant. Spectrosc. Radiat. Transf. **81**, 287 (2003).
[34] J. J. MacFarlane, G. A. Moses, and R. R. Peterson, *Bucky-1: A 1-D Radiation-Hydrodynamics Code for Simulating Inertial Confinement Fusion* (University of Wisconsin FTI, Madison 1995).
[35] G. L. Olson and P. B. Kunasz, J. Quant. Spectrosc. Radiat. Transf. **38**, 325 (1987).
[36] G. A. Rochau, Ph.D. thesis, University of Wisconsin (unpublished).